

**Formation of hydrothermal deposits at Kings Triple Junction, northern
Lau Back-arc basin, SW Pacific: The geochemical perspectives**

Anil L. Paropkari ^{a*}, Durbar Ray ^a, Balaram V. ^b, Surya Prakash L. ^a,
Imran H. Mirza ^a, Satyanarayana M. ^b, Gnaneshwar Rao T. ^b, Sujata Kaisary ^a

^a *National Institute of Oceanography, (CSIR), Goa-403004, India.*

^b *National Geophysical Research Institute, (CSIR), Hyderabad-500007, India.*

Abstract

An inactive hydrothermal field was discovered near Kings Triple Junction (KTJ) in northern Lau back-arc basin during 19th cruise of R/V *Akademik Mstislav Keldysh* in 1990. The field consisted of a large elongated basal platform ‘the pedestal’ with several ‘small’ chimneys on its periphery and one ‘main mound’ superposed over it. The surrounding region is carpeted with lava pillows having ferromanganese ‘precipitate’ as infillings. The adjoining second field consisted of small chimney like growths termed as “Christmas Tree” Field. The basal pedestal, the peripheral chimneys and small “Christmas Tree” like growths (samples collected by *MIR* submersibles), though parts of the same hydrothermal field, differ significantly in their mineralogy and elemental composition indicating different history of formation. The pedestal slab consisting of chalcopyrite and pyrite as major minerals and rich in Cu is likely to have formed at higher temperatures than sphalerite dominated peripheral chimney. Extremely low concentration of high field strength elements (e.g. Zr, Hf, Nb and Ta) and enrichment of light REE in these sulfides indicate prominent influence of aqueous arc-magma, rich in subduction components. The oxide growths in the “Christmas Tree” Field have two distinct layers, Fe rich orange-red basal part which seems to have formed at very low temperature as precipitates from diffused hydrothermal flows from the seafloor whereas Mn rich black surface coating is formed from hydrothermal fluids emanated from the seafloor during another episode of hydrothermal activity. Perhaps this is for the first time such unique hydrothermal oxide growths are being reported in association with hydrothermal system. Here, we discuss the possible processes responsible for the formation of these different hydrothermal deposits based on their mineralogy and geochemistry.

Keywords: Lau basin; Hydrothermal Field; Chimney; Mineralogy; Geochemistry;

* *Corresponding Author:* Dr. A. L. Paropkari, National Institute of Oceanography, Goa, India. Tel.: 91-832-2450336; Fax: 91-832-2450609; E-mail: parop@nio.org

An edited version of this paper was published by Elsevier. Copyright [2010] Elsevier

1. Introduction

The back-arc and marginal basins in south-west Pacific Ocean (e.g. Okinawa Trough, Mariana Trough, Manus Basin, Lau Basin, North Fiji Basin, Woodlark Basin), are well known for sea floor hydrothermal activity and associated massive sulfide deposits (Hawkins and Helu, 1986; Gamo et al., 1993; Lisitzin et al., 1997; Herzig et al., 2000; Glasby and Notsu, 2003). During the 19th cruise of R/V *Akademik Mstislav Keldysh* in May, 1990 hydrothermal fields of Lau basin have been explored thoroughly with MIR submersibles. Massive sulfide and associated andesitic lava (Falloon et al., 1992) were collected from two locations, one from an extinct field (Lau-North) while another was active (Lau-Centre) (Lisitsyn et al., 1992). Here we deal with the samples collected from the northern part of the Lau basin. As this region is characterized by the presence of an inactive field, the hydrothermal fluid characteristics could not be determined. Based on shipboard analyses, Lisitsyn et al. (1992) preliminarily described the geochemical characters of these deposits and inferred that hydrothermal activity here might have ceased in the recent past. Nevertheless as these data are very limited, we undertook detailed mineralogical and geochemical investigations on three types of samples collected from this field to understand the formation of these hydrothermal deposits.

2. Geophysical setting and description of the hydrothermal field

The Lau basin, a trapezoidal-shaped back-arc basin, separating the Lau ridge from Tonga volcanic island-arc, is located near the Pacific and Indo-Australian convergent plate boundary. In the northeastern part of this basin, three well defined spreading axes meet at a ridge-ridge-ridge type triple junction (Hawkins, 1995) known as Kings Triple Junction (KTJ) or Mangatolu Triple Junction (MTJ) (15°30'S, 174°35'W, Fig. 1). *Geological LOng Range Inclined Asdic* (GLORIA) side-scan sonar surveys showed that the KTJ consist of three overlapping spreading centers and a transform fault (Parsons et al., 1989; Falloon et al., 1992). The KTJ and its surroundings have a complex geophysical setting associated with both volcanic arc and oceanic ridge like features lying in close proximity. The axial ridge has narrow rift valley which gradually deepen away from KTJ (Lisitsyn et al., 1992). Combined airborne magnetic data, bathymetry and GLORIA images showed that the KTJ has smooth summit with rougher terrain and deep overlapping fissures radiating out to the south and further suggested the presence of a shallow magma chamber (Malahoff and Falloon, 1991). These features combined with the occurrence of apparently fresh smooth surficial lava flows indicate the possibility of recent hydrothermal activity in this region (Malahoff and Falloon, 1991). Parson and Tiffin (1993) also describe the KTJ as an intensely deformed neovolcanic area.

During the cruise five dives were undertaken at four sites by 'MIR' submersibles (*MIR I* and *MIR II*) in the northwestern part of Lau basin (Fig. 1) (Lisitsyn et al., 1992, 1997; Malahoff and Fallon, 1991, Falloon et al., 1992). Among the four *MIR* dives in Lau basin, dive M-2226 was conducted near KTJ (15°23.2'S, 174°40.1'W) over northwest spreading ridge (Fig.1) of the triple junction (Falloon et al.1992). During this dive a huge “dead” hydrothermal field was discovered (Lysitsyn et al., 1992) on the central high of an axial ridge graben at 2050 m water depth. This field has length of 2000m and width of 200m. At the center of this hydrothermal field, a huge elliptical ‘pedestal’ (100 m in length, 30-50 m in width and ~20 m in height) elongated in north-south direction with central hydrothermal mound (~10m height) was found. The sample M-2226-5 (pedestal slab) represents the portion of the surface of the pedestal. The pedestal also had several columnar chimneys of height 1.0–2.0 m on its periphery and the sample M-2226-6/12 represents a section of one of these standing peripheral chimneys (Fig. 2). Along the outer rim of this field, the seafloor mainly comprised of basalt pillows with unconsolidated yellowish-brown deposits accumulated in the hollows between them (Fig. 2). A second hydrothermal field having precipitates in the form of small vertical structures (50-70 cm height) resembling the “Christmas Tree” in shape and consisting of orange-red dusty fragile material with black surface coating (1.0 -1.5 cm thick) were observed in the nearby region. The sample, M-2226-12 was obtained from a structure of this type.

3. Materials and methods

For the present investigation, representative samples of three different formations (pedestal slab, peripheral chimney and Fe and Mn precipitate), (Fig. 3) were selected.

3.1. Sample description and preparation

The sample of pedestal slab (M-2226-5) is characterized by concentric layering with distinct colour variations including shades of grey, dark black and red. Four sub-sections of this sample were made based on colour variations as shown in the Fig. 3A. Based on the description of the pedestal slab (Lisitsyn et al., 1992) layer L-1 represents deeper zone while L-4 is the topmost layer. The sample M-2226-6/12 is a section from 70cm tall peripheral chimney (Lisitsyn et al., 1992) which had one orifice and a small conduit channel (Fig. 3B). This sample was very hard and displayed gray shade without any concentric patterns. Due to absence of any colour pattern, sub-sectioning of the sample was done at every 1.5 cm with reference to the orifice (S-5) as shown in the Fig. 3B. The section S-6 contained a narrow conduit and showed crystallized dark minerals on its interior wall. The vertical precipitate (sample M-2226 -12) had two distinct layers, orange basal part termed as ochre (O-12) and black coating (B-12) on surface (Fig. 3C). Samples from two layers were analyzed separately.

3.2. Mineralogical analysis

Powdered samples were analyzed for mineralogical composition with a Philips PW-1840 X-ray diffractometer. Samples were scanned using Cu-K α radiation over 2 θ range from 5° to 60°. The mineralogical interpretation of X-ray diffractograms was done using Traces® software to assign 2 θ values.

3.3. Bulk chemical analysis

For chemical analysis, 50mg of powdered sub-samples were mixed with 10ml acid mixture (HF: HNO₃: HClO₄: 7:3:1) and then evaporated to complete dryness. To this 20ml (1:1) ultra pure nitric acid was added and final volume made up to 250ml with Milli-Q water. Trace and rare earth elements were analyzed with ICP-MS (Perkin Elmer SCIEX ELAN® DRC-II) using 20ng/ml Rh¹⁰³ as internal standard (Balaram and Gnaneshwar Rao, 2003). Standard reference material, IF-G (from Groupe International de Travail, France) was used for instrument calibration and the analytical precision with <5.0% RSD were achieved. The analysis of Mn, Fe, Cu, and Zn in the same solutions was carried out using Perkin-Elmer® AAS (Model Aanalyst-200) with SCO-1, SGR-1, BCSS, MESS as reference standards.

To determine gold and silver content, 2.0g of the finely powdered samples were digested with aqua-regia in Teflon® beakers and then final volumes were made up to 100ml and diluted further before ICP-MS analysis. International gold ore reference materials S-5 and OX-11 (from Rock labs Ltd., New Zealand) were used for calibration.

4. Results

4.1. Pedestal slab (sample M-2226-5)

The deeper layers L-1 and L-2 of the pedestal slab display significant enrichment of chalcopyrite, pyrite, and barite with minor presence of sphalerite, wurtzite and manganosite (Table 1). The intermediate L-3 layer differs from L-1 and L-2 and has abundant sphalerite with traces of chalcopyrite. The topmost surface layer, L-4 mostly contains chalcopyrite. Layers L-1, L-2 and L-4 show high concentration of Cu (av. 11.73%) and Fe (av. 9.74%) followed by Zn (av. 3.56%) and Mn (av. 0.01%) whereas the black colored L-3 is relatively enriched in Zn (24%) and Mn (0.026%) but low in Cu (4.48%), and Fe (2.87%) (Table 2). Trace elements (e.g. Rb, Y, U), low ionic radii lithophillic elements (LILEs - Ba, Sr) and high field strength elements (HFSEs – Zr, Nb, Hf, Ta) also

have relatively low concentration in L-3 (Table 2), which exhibits considerable enrichment of Au (2.82ppm) and Ag (15.48 ppm).

Layers L-1, L-2 and L-4 have relatively high total REEs (Σ REE) contents (16.34, 7.39, and 5.86ppm respectively) and pronounced positive Eu anomalies (Table 3; Fig. 4A). L-3 which is characterized with minimum REE (Σ REE = 0.9 ppm) has least positive Eu anomaly ($Eu_n/Sm_n = 20$), but maximum light to heavy rare earth element fractionation ($Nd_n/Yb_n = 4.18$).

4.2. Peripheral chimney (sample M-2226-6/12)

In the peripheral chimney sample, the major mineral suite consists of sphalerite, with minor presence of pyrite, chalcopyrite, and manganosite (Table 1). No anhydrite was detected in any section of this chimney sample. Chimney sub-sections have similar mineralogical composition but the relative abundance of sphalerite against chalcopyrite increases slightly from the orifice (S-5) towards the periphery (S-1). The mineralogy is well reflected in chemical composition with major contribution by Zn (23-34%), followed by Fe (1.2- 4.3%), Cu (1.0-1.5%) and Mn (0.03-0.06%) (Table 2). Trace elements (e.g. Rb, Y, U), LILEs (Ba, Sr) and HFSEs (Zr, Nb, Hf, Ta) exhibit relatively low concentration at the orifice (S-5) (Table 2). Sulfides in chimney sample are relatively rich in Au (1.6 to 5.7 ppm) and Ag (12.2 to 35.4 ppm).

The total REE (Σ REE) content of all the sections shows minor variation, having least concentration (0.65ppm) in orifice section S-5 and maximum (1.12 ppm) at outermost section S-1 (Table 3). Chondrite (C-1) normalized REE patterns (Fig. 4B) of all sections are similar to pedestal slab layers with prominent positive Eu anomalies ($Eu_n/Sm_n = 2.3-5.5$) and substantial enrichment of LREE relative to HREE ($Nd_n/Yb_n = 3.1$ to 5.5).

4.3. The Fe and Mn oxide precipitates (sample M-2226-12)

X-ray diffraction studies of surface black layer (B-12) revealed the presence of poorly crystalline 7Å manganate (birnessite) whereas orange colored 'ochre' (O-12) did not show any peak indicating its amorphous nature (Table 1). The sample B-12 is rich in Mn (32.19%) while sample O-12 is rich in Fe (14.52%) (Table 2). B-12 is also relatively enriched with Ni, Zn and LILEs (Ba, Sr) but has less HFSEs (Zr, Nb, Hf, Ta) concentrations. Compared to sulfides of the pedestal slab and chimney, these precipitates have higher uranium concentrations with a maximum of 1.85 ppm in B-12 sample.

Chondrite normalized REE patterns (Fig. 4C) of both the precipitates have significant negative Ce anomalies (0.42 and 0.36, Table 3) and minor positive Eu anomaly ($Eu_n/Sm_n=2.5$ and 3.3). The ΣREE of these two samples O-12 and B-12 are quite low, 1.9 and 1.6 ppm respectively (Table 3). These hydrothermal precipitates show trivial fractionation between light and heavy rare earth elements ($Nd_n/Yb_n=1.2$).

5. Discussion

Several earlier investigations have shown that the influence of fluid temperature, composition and crystallographic effects control the distinct zonations of minerals and elemental distributions in different hydrothermal deposits (Francheteau et al., 1979; Haymon and Kastner, 1981; Hannington et al., 1991; Von Damm, 1995; Herzig and Hannington, 2000). It is also well known that hydrothermal formations in back-arc settings are influenced by supra subduction zone (SSZ) melts that are characterized by enrichment and/or depletion of certain trace metals and are therefore distinct from those found on mid-ocean ridges (Shanks III, 2001). These concepts form the basis for the present interpretation of the geochemical environment that might have prevailed during the formation of these hydrothermal deposits.

5.1. Formation of the pedestal slab

5.1a. Signatures of subduction induced high temperature melt

Earlier studies showed that massive hydrothermal sulfides, consisting of chalcopyrite and pyrite minerals and rich in Cu, are most likely to have formed under high temperature ($>300^{\circ}$ - 400° C) conditions (Fouquet et al., 1991, Kim et al., 2006). Thus, the considerable enrichment of Cu (4-16 wt%) and Fe (3-12 wt%) in the pedestal slab samples having chalcopyrite and pyrite as major minerals (Table 1) indicate their formation at very high temperature.

The pedestal slab layers show overall enrichment of low ionic radii lithophilic elements (LILEs) (e.g. Ba=100-10,000ppm, Sr=5-180ppm) and LREEs, La=0.2-3.2ppm) but minimum accretion of high field strength elements (HFSEs) (e.g. Zr<1.0ppm, Hf<0.1ppm, Nb<0.6ppm and Ta<0.25ppm) (Table 2). Commonly, during subduction-related hydrous melting, LILEs prefer mobile fluid phase while the HFSEs are known for their conservative nature. Recent study shows that barite-rich volcanic massive sulfide in central part of mature arc system are acquiring LILE from calc-alkalic magmatism (Sawkins, 2009). The andesitic lava recovered from KTJ (Falloon et al., 1992) is result of calc-alkalic magmatism, which might have supplied volatiles, notably water and LILE to the sulfide of pedestal slab. Thus, the formation of the pedestal slab layers could be related to precipitation of the fluids from

typical hydrous back-arc basin magma with subduction components. This is consistent with earlier petrological investigations at KTJ which also revealed prominent impregnation of SSZ mantle (Hawkins, 1995). High Ba to Nb ratios (a proxy for total subduction inputs; Paerce and Stern, 2006,) in the pedestal slab ($Ba/Nb=10^3-10^5$, Table 2) also indicate substantial contribution from subduction melt. Cs is another highly mobile element, normally found to be associated with arc volcanism ($Cs=0.7-2.0ppm$) rather than unaltered MORB ($Cs=0.0086ppm$; Hawkins, 1995). Thus, high concentrations of Cs (0.2-1.9ppm, Table 2) in this slab resemble those in the melts originating from the SSZ setting.

5.1b. Elemental distributions: Effects of crystallography and zone refinement

Our investigation reveals that the mineralogy and the chemical composition of different layers in the slab are not uniform. According to Tivey et al. (1995), such zonal variations of minerals and associated elements occur mostly due to zone refinement processes induced by seawater entrained within a hydrothermal mound. This includes conductive cooling of entrained seawater circulating in deeper part of the mound that precipitates pyrite, chalcopyrite and simultaneously generates more acidic fluid, resulting in dissolution of sphalerite. Under these conditions, dissolved zinc sulfide (ZnS , sphalerite) is prone to remobilization (Wagner and Cook, 1998). Whenever, zinc sulfide dissolves and mobilizes, associated elements like Ag, Au and Ga are also expected to remobilize and deposit in near surface low temperature zone. In our results, the sphalerite dominated L-3 and partly the surface layer L-4 was found to be relatively rich with Zn, Ga, V, Ag, and Au probably due to effect of remobilization, influenced by seawater entrained within the mound. In contrast, the deeper layers L-1 and L-2 are likely contain high temperature sulfides which are depleted in Zn and associated trace elements. A similar observation of high temperature pyrite in deeper part of TAG hydrothermal mound has been reported by Fouquet et al. (1998). Barite is the only sulfate phase present in these deeper layers but no anhydrite has been detected as has been reported in active hydrothermal mounds (Hannington et al., 2001; Mills and Elderfield, 1995). This absence of anhydrite is attributed to the retrograde solubility wherein anhydrite within the mound would re-dissolve at low ambient temperature as activity ceases (Haymon and Kastner, 1981, James and Elderfield, 1996, Fouquet et al., 1998). The coexistence of barite with sulfide minerals in deep layers L-1 and L-2 suggest substantial contributions of infiltrated seawater.

In general, incompatibility of REEs in sulfide lattice (Mills and Elderfield, 1995) and fast rate of precipitation make hydrothermal deposits quite low in REE content. In the present study, although all four layers had quite low REE content, there was considerable variation in $\Sigma REEs$. It is interesting to

note that, the deep layers L-1 and L-2 with pristine Cu-Fe sulfides (pyrite and chalcopyrite) have high REE content ($\Sigma\text{REE}=16.3$ and 7.4 ppm respectively) with a maximum Eu contribution (more than 50%). In the absence of any specific REE mineral, we attribute this contrasting result to a considerable sink of REEs in sulphate phase, mainly barite, detected in both layers. The comparable solubility of BaSO_4 and EuSO_4 (Graff, 1977) along with substitution of Sr^{+2} and Ba^{+2} with compatible Eu^{+2} in barite lattice (Morgan and Wandless, 1980) would be responsible for marked Eu anomalies. Besides Eu, concentrations of La and Ce are significantly high and have major contribution towards total REE of layers L-1 and L-2 (Table-3). The REE patterns of all four layers normalized to chondrite (C-1) (Fig. 4A) clearly show LREE enrichment compared to heavier ones and resemble typical hydrothermal deposits. But the degree of this cross group fractionation is less pronounced ($\text{Nd}_n/\text{Yb}_n < 2$) in L-1 and L-2 compared to L-3 and L-4 ($\text{Nd}_n/\text{Yb}_n > 3$). This is also possible as a consequence of zone refinement processes, which preferentially removes mobile LREE into fluid phase and redeposit them at top layers. Moreover, low REE content ($\Sigma\text{REE} = 0.9\text{ppm}$) and REE pattern (Fig. 4A) of sphalerite dominated L-3 differ from other three Cu-Fe-sulfide rich layers ($\Sigma\text{REE} > 5.8\text{ppm}$ & Fig. 4A) but resembles to that of chimney sections ($\Sigma\text{REE} = 0.7-1.1\text{ppm}$ & Fig. 4B). This indicates that, besides zone refinement, crystallographic control of REE incorporation in sulfide lattice is also effective for such elemental distributions. This is supported by the results of Mills and Elderfield (1995) wherein distribution coefficient (K_D) of REE between sulfide and fluid phase revealed that hydrothermal sphalerite having prominent crystallographic control is depleted in REE compared to chalcopyrite which has minimum crystallographic control on REE incorporation.

5.2. Formation of peripheral chimney

5.2a. Evidences for low temperature formation

Sphalerite rich chimneys with traces of pyrite and chalcopyrite observed in the present investigation with typical columnar structure on the periphery of pedestal slab resemble to low temperature 'white smokers' described by Koski et al. (1994) and Paradis et al. (1988) rather than Cu-Fe rich high temperature ($>300^\circ\text{C}$) black smokers (Kim et al., 2004). Two small and narrow conduit channels (S-5 and S-6 in Fig. 3B) with rugged internal wall near the outer rim of the chimney indicates the passage of less buoyant and gentle fluid typical of the formation of a low temperature white smoker chimney unlike the large orifice associated with vigorous buoyant flow of a black smoker. Similar multiple, narrow, tortuous flow conduits were found in white smokers from TAG field (Tivey et al., 1995).

Low Cu (max 1.5%) and Fe (max 4.3%) content of this sample indicates low temperature formation. Furthermore, in this sphalerite rich sample considerable accretions of Zn, V, Ga, Zr, Hf, Ag and Au,

elements which normally precipitate at lower temperature, is analogous to relatively cooler white smoker chimneys described by Koski et al. (1994), Tivey et al. (1995), Kim et al. (2004). The homogeneous nature of the chimney subsections is also reflected in their identical chondrite (C-1) normalized REE patterns (Fig. 4B). All the chimney sections are characterized by enrichment of LREEs ($Nb_n/Yb_n=2.6-5.4$; Table 3) comparable to sphalerite from white smoker ($Nb_n/Yb_n=4.19$, Mills and Elderfield, 1995) from TAG hydrothermal mound. Sulfide of peripheral chimney had less positive Eu anomaly ($Eu_n/Sm_n=4.0\pm 1.2$, Table 3, Fig. 4B) also confirming its low temperature formation. Thus morphology and geochemistry of this chimney are strikingly similar to white smokers chimneys reported elsewhere (Koski et al., 1994; Tivey et al., 1995; Mills and Elderfield, 1995).

5.2b. Elemental distributions: Physiochemical conditions during chimney growth

In the chimney sample, no concentric mineral zoning around the orifice was found as reported by Haymon and Kastner, (1981); Tivey et al. (2004), Jianbin et al. (2007). Sulfide mineral zoning in chimneys normally occur in response to change in temperature and composition of hydrothermal fluid (Haymon and Kastner, 1981; Janecky and Seyfried, 1984). Thus almost uniform mineralogical composition of the chimney section indicates that there was no major change in fluid temperature and composition during the chimney growth. But interestingly some of the trace elements (e.g. Sc, Rb, Au, Ag, Th, U), LILEs (Ba, Sr), and HFSEs (Zr, Hf, Nb, Ta) had the least concentrations around the orifice (S-5) while these gradually increased towards the wall (S-1) (Table-2). The significant enrichment of trace elements especially at chimney outer sections (S-1 and S-2) is perhaps due to relatively low temperature mineral precipitation during initial chimney development. In early growth phases, such sphalerite rich chimneys are dominated by porous dendritic sulfides that keep the chimney wall cooler (Koski et al., 1994). As the chimney matures, slow precipitation of colloform sulfides and amorphous silica gradually make the wall thicker and less porous, ultimately raising the internal temperature of the orifice (Halbach and Munch, 2000; Xiatong and Hnaiyang, 2005). Marginal increase in relative abundance of chalcopyrite around the orifice (S-5) is consistent with this. Thus, mature consolidated chimney maintains warm conditions and that in turn keeps most of the trace elements in residual solution and decreases their accretion near the orifice

5.3. Formation of Fe and Mn oxide precipitates

5.3a. Evidences of hydrothermal origin

Hydrothermal ferromanganese deposits are usually formed due to precipitation of hydrothermal plume particulates or by oxidation of diffused fluid flows through the fractures on the sea floor (Mills et al., 2001; Bautier et al., 2004,). Several hydrothermal deposits having characteristic phyllosulfate and

amorphous Fe-oxyhydroxides were reported along central Valu-Fa Ridge in southern Lau basin, (Fouquet et al., 1993; Daessle et al., 2000) and other active hydrothermal fields (Francheteau et al., 1979; Natland et al., 1979; Haymon and Kastner, 1981; Moorby et al., 1984). These Fe-Mn-oxides normally found as metalliferous encrustations or thin unconsolidated oxide coatings on the sea floor in the surrounding region of the hydrothermal provinces. In the present study, we have identified unique oxide growths in the 'Christmas Tree' field having two distinct layers (as described above) which have not been reported from any other hydrothermal field. Based on the morphology, mineralogy and geochemistry we would propose the following mechanism of their formation. Malahoff and Falloon, (1991) referred these kind of growths as nontronite chimneys but our results do not show any characteristic peak of nontronite in either of these two sub-samples, B-12 and O-12. Similarly, Lisitsyn et al. (1992) also did not find significant nontronite presence, except rare occurrence in some samples, and found that the orange colored Fe-rich bottom part (O-12) is devoid of any prominent X-ray diffraction peak revealing its amorphous nature, as also observed by us. This orange amorphous part being rich in iron, we believe this could form by direct precipitation of Fe-oxides and oxyhydroxides from fluid ascended through scattered fissures or fractures near the main mound over a period of time. Two processes, either oxidation of Fe^{+2} or hydrolysis of Fe^{+3} , leads to such Fe-oxide precipitation (Murray, 1979). The precipitation of hydrothermal solution via kinetically controlled Fe^{+3} hydrolysis is slow and results in formation of minerals like goethite, lepidocrocite, ferrihydrite and hematite (Pichler and Veizer, 1999). But presence of the X-ray amorphous FeOOH in sample O-12 indicates its rapid precipitation, possibly due to instantaneous oxidation of Fe^{+2} in hydrothermal solutions emanated through factures within pillow basalts near the mound. In contrast, surface black layer, B-12 shows the presence of birnessite, stable 7Å manganate, which might have formed later either due to precipitation of Mn-rich plume particulate during subsequent episodes of hydrothermal activity or these could have formed due to changed composition of hydrothermal fluid. This formation issue of manganese encrustations will be resolved using the geochemistry, particularly the REEs of these deposits, as follows.

Bulk geochemical analysis of these Fe and Mn oxides show very low concentration of Zn (<200 ppm), Cu (~100 ppm), Ni (<100 ppm), and Co (<4.0 ppm) and resemble to the typical hydrothermal deposits rather than deep sea hydrogenous crust (Usai and Someya, 1997). The fast growth rate of hydrothermal Fe and Mn oxides (>1000mm/Myr) does not allow much accretion of these trace elements from ambient seawater. Furthermore, extremely low rare earths contents (ΣREE <2.0 ppm) also indicates less interaction with seawater, providing minimum scope for scavenging of REE from seawater. Compared to sulfides, these oxides have relatively flat REE patterns (Fig. 4C) with

negative Ce and minor positive Eu anomalies. According to mode of formation, Mills et al. (2001) classify hydrothermal Fe-Mn oxides from the TAG hydrothermal mound based on REE fractionations, with minimum value ($Nd_n/Yb_n \sim 1$) for low temperature fluid precipitation and higher fractionation ($Nd_n/Yb_n > 3$) for plume derived precipitates. Thus, negligible REE fractionation ($Nd_n/Yb_n = 1.2$) in both layers suggest direct precipitation of reduced hydrothermal fluids emanated through fractures within pillow basalts would be responsible for such oxide growths. Moreover, this finding rules out the possibility of the formation of Mn oxide (B-12) encrustations due to hydrothermal plume precipitation.

5.3b. Elemental distributions: Control of Fe and Mn oxide precipitates

These Fe and Mn oxides (O-12 and B-12) are characterized with extreme contrasting Fe to Mn ratio ($Fe/Mn = 160$ and 0.041 respectively). Results show that Fe-rich O-12 has extremely low concentration of Mn (0.089%). It is proposed that such Fe-rich hydrothermal oxides, devoid of crystalline phase, form due to direct precipitation of Fe-saturated solution on sea floor, following oxidation of Fe^{+2} during mixing with alkaline, oxygenated sea water (Pichler and Veizer, 1999). Lack of sufficient Mn oxidation and a decreased chance of crystallographic substitution of Fe^{+3} with Mn^{+3} causes Mn depletion in sample O-12. In contrast, B-12 with Mn oxide in the form of birnessite has significant Fe ($< 1.5\%$) and may indicate preferable replacement at the specific sites of phyllo-manganate crystals with noncrystalline Fe-oxyhydroxide. Moorby and Cronan, (1981) has also reported similar crystallographic effect in other hydrothermal ferromanganese deposit.

Compared to Fe-oxyhydroxide (O-12), the Mn-oxide in B-12 is enriched with Ni and Zn but low in Co (Table 2). This could be attributed to the preferential partitioning of these elements in different oxide phases as reported in other ferromanganese crusts from Valu Fa Ridge (Daessle et al., 2000) and Tonga–Kermadec sites (Moorby et al., 1984). In seawater (pH-7.8), the Mn-oxide collides ($pH_{zpc} = 2.0-2.8$, Stumm and Morgan 1981) of suspended particulates would develop negative surface potential and preferentially attracts positively charged species. Elements like Ni, Zn, Ba, Sr, Rb mostly existing as complex or free cations in seawater and hydrothermal fluid, get strongly sorbed on negatively charged Mn-oxide precipitates. Concentration of U in these oxides especially in the top black crust (B-12) is significantly high (1.8 ppm). More efficient incorporation of U in Mn hydroxides than in Fe hydroxides (Marchig, 2000) and sluggish oxidation kinetics of Mn^{+2} , facilitate U enrichment in B-12. Unlike other trace elements, distribution of REE in these two oxide phases does not vary much. This demonstrates minimum control of Fe-Mn abundance and their mineralogy on REE systematics.

Previous studies on ferromanganese crusts of TAG field by Mills et al. (2001) also could not find any correlation between bulk REE contents and Fe/Mn ratio or any mineralogical control on REE patterns.

6. Development of the Lau hydrothermal field:

Based on the constraints imposed by the mineralogical and geochemical data and on morphological characters, a simple model for the growth and evolution of the TAG active hydrothermal mound has been envisaged (Tivey et al., 1995, Humphris and Kleinrock, 1996). We attempt here to utilize this information to deduce the formation history of the Lau hydrothermal field based on the striking similarity in mineralogy, geochemistry and morphology of Lau field with the TAG field despite differences in their tectonic settings.

The Lau field has a cone shaped 'main mound' structure superposed on the broader of discrete flat platform, termed as 'pedestal slab'. This conical 'main mound' is a massive sulfide structure resting on the pedestal and is characterized by presence of numerous tubes on its summit and its side walls (Lisitsyn et al., 1992). This description of mound matches well with the cone-shaped structure on TAG mound having black smoker complex which vigorously discharge high temperature fluids (Tivey et al., 1995, Humphris and Kleinrock, 1996). Such sulfide structure indicates rapid and well focused fluid flow from the sea floor. We could not analyze a sample from the cone due to paucity of a sample. But the reported mineralogical composition chalcopyrite, bornite, covellite of this 10m high cone indicates very high temperature formation (Lisitsyn et al., 1992) and support the above inferences. The mineralogical and chemical composition of the pedestal slab sample matches well with that of massive hydrothermal sulfide that is likely to have formed during high temperature fluid flow through permeable basement as pointed out by Tivey et al. (1995) for TAG mound. The same inference has been drawn by Lisitsyn et al. (1992) who suggested high temperature formation of pedestal.

Several scattered small sphalerite chimneys along the periphery of pedestal slab are very similar to Zn-rich white smokers in "Kremlin field" of the TAG area (Tivey et al., 1995). White smoker fluid which results from the subsurface mixing of hydrothermal fluid and cold seawater entrained beneath the mound discharges through the edge of the mound forming these chimneys. The morphology, internal structure, chemistry and mineralogy of these chimneys from peripheral part of pedestal slab very much resemble to the white smokers of 'Kremlin field' (Tivey et al., 1995) and therefore we believe that these are the remnant 'white smokers'. Preliminary inference drawn by Lisitsyn et al. (1992) also terms these chimneys as white smokers.

None of the hydrothermal deposits reported so far have discovered the oxidized deposits as observed in Lau deposits in ‘Christmas Tree’ field having distinctly two separate layers. Earlier, Tivey et al. (1995) reported occurrence of ocherous material that formed during hydrothermal episodes exposed on the steep outer walls of the TAG mound due to oxidation of sulfide by a low temperature hydrothermal fluid combined with primary precipitation of Fe oxide and silica from this same fluid. The oxide growths of ‘Christmas Tree’ field also having ocherous Fe-rich oxides in its lower part. It is likely that the Fe-oxide chimneys were built by low temperature hydrothermal fluids emanating from the floor during hydrothermal activity. These were subsequently capped by the Mn-oxides derived from the oxidation of Mn-rich fluid discharged from seafloor during subsequent episode of hydrothermal activity.

7. Conclusions

Three samples representing three different hydrothermal structures from the extinct site near KTJ of northern Lau back-arc basin differ from each other in terms of their basic mineralogy, bulk elemental composition and REE systematics, suggesting different history of formation. Although same source fluid may be responsible for all three formations but different concentration of elements like Fe, Cu, Zn, Sr, Ba, Ga, Ag and REE, variety of Eu and Ce anomalies, different degree of REE fractionation indicate significant sub-seafloor alteration of source fluid prior to precipitation of these structures. The sulfide mineralogy, enrichment of Fe, Cu, Ba, very large positive Eu anomalies in pedestal slab resemble typical high temperature hydrothermal deposits while peripheral chimney made up of sphalerite and rich in low temperature elements like Zn, Ga, Ag, Au is likely to have formed at comparatively low temperature. The “Christmas Tree” like Fe and Mn oxide precipitates are formed due to very low temperature fissure emissions of hydrothermal fluid in the near by region. Very fast oxidative precipitation of low temperature hydrothermal fluid emanating through the fissure openings, with change in fluid composition, possibly results in formation of such oxide structures having two distinct layers.

It is interesting to note that despite the difference in the tectonic setting in Lau and TAG fields, the overall process of the formation of hydrothermal mounds seem to be very similar. However, the temperature of expelling fluids, sub-seafloor water-rock and hydrothermal fluid convecting seawater interactions control the elemental abundance and distribution in such deposits and are perhaps the most important factors determining their mineralogy and geochemistry.

Acknowledgements

The authors are thankful to the Director, National Institute of Oceanography, and the Director, National Geophysical Research Institute, for their encouragement. The first author is highly grateful to the chief scientist Academician Prof. Alexander. P. Lisitsyn for inviting him to participate in the cruises of R/V *Akademik Mstislav Keldysh* and providing the samples collected by *MIR* submersibles to undertake the investigations. We are also grateful to Dr. K. A. Kamesh Raju, Project Leader, for his constant support and to Mr. Girish Prabhu for XRD analysis. We thank two anonymous reviewers for their valuable comments on the manuscript. This is NIO's contribution no. ----.

References

Balaram, V., Gnaneshwar Rao, T., 2003. Rapid determination of REEs and other trace elements in geological samples by microwave acid digestion and ICP-MS. *Atomic Spectroscopy* 24 (6), 206-212.

Daessle, L.W., Cronan, D.S., Marchig, V., Wiedicke, M., 2000. Hydrothermal sedimentation adjacent to the propagating Valu Fa ridge, Lau basin, SW Pacific. *Marine Geology* 162, 479–500.

Falloon, T. J., Malahoff, A., Zonenshain, L. P., Bogbanov, Y., 1992. Petrology and Geochemistry of Back-arc Basin Basalt from Lau Spreading Ridges at 15°, 18° and 19°S. *Mineralogy and Petrology* 47, 1-35.

Fouquet, Y., Von Stackelberg, U., Charlou, J. L., Donval, J.P., Erzinger, J., Foucher, J. P., Herzig, P., Muhe, R., Soakai, S., Wiedicke, M., Whitechurch, H., 1991. Hydrothermal activity and metallogenesis in the Lau back arc basin. *Nature* 349, 778-781.

Fouquet, Y., Von Stackelberg, U., Charlou, J.L., Erzinger, J., Herzig, P.M., Mühe, R., Wiedicke, M., 1993. Metallogenesis in back-arc environments: the Lau Basin example. *Economic Geology* 88, 2154-2181.

Fouquet, Y., Henry, K., Knott, R., Cambon, P., 1998. Geochemical section of the TAG hydrothermal mound. in *Proceedings of the Ocean Drilling Program, Scientific Results*, (Eds.), Herzig, P.M., Humphris, S.E., Miller, D.J., and Zierenberg, R.A., Vol. 158, pp. 363-387.

Francheteau, J., Needham, H.D., Choukroune, P., Juteau, T., Seguret, M., Ballard, R.D., Fox, P.J., Normark, W., Carranza, A., Cordoba, D., Guerrero, J., Rangin, C., Bougault, H., Cambon, P.,

Hekinian, R., 1979. Massive deep-sea sulphide ore deposits discovered on the East Pacific Rise. *Nature* 277, 523-528.

Gamo, T., Sakai, H., Ishibashi, J., Nakayama, E., Isshiki, H., Matsuura, H., Shitashima, K., Takeuchi, K., Ohta, S., 1993. Hydrothermal plumes in the eastern Manus Basin, Bismarck Sea: CH₄, Mn, Al and pH anomalies. *Deep Sea Research Part - I* 40 (11/12), 2335-2349.

Glasby, G. P., Notsu, K., 2003. Submarine hydrothermal mineralization in the Okinawa Trough, SW of Japan: an overview. *Ore Geology Review* 23, 299–339.

Graff, J. L., 1977. Rare earth elements as hydrothermal tracers during the formation of massive sulfide deposits in volcanic rocks. *Economic Geology* 72, 527-548.

Halbach P., Munch U., 2000. Mineral Deposits at 23°S, Central Indian Ridge: Mineralogical Features, Chemical Composition and Isotopic Investigations. In: Cronan D. S. (Ed), *Handbook of Marine Mineral Deposits*, CRC press USA, pp.327-346.

Hannington, M., Herzig, P., Stoffer P., Scholten J., Botz R., Garbe-Schonberg D., Jonasson I.R., Roest w., Shipboard Scientific Party, 2001. First observations of high-Temperature submarine hydrothermal vents and massive anhydrite deposits off the north coast of Ice land. *Marine Geology* 177, 199-220.

Hannington, M., Herzig, P., Scott, S., Thompson, G., Rona, P., 1991. Comparative mineralogy and geochemistry of gold-bearing sulfide deposits on the mid-ocean ridges. *Marine Geology* 101, 217-248.

Hawkins, J., Helu, S., 1986. Polymetallic sulfide deposit from “black smoker” chimney: Lau basin. *EOS (Transactions, American Geophysical Union)* 67, 378.

Hawkins, J. W. 1995. The Geology of the Lau Basin. In: Brian Taylor (Ed) *Backarc Basins - Tectonics and Magmatism*. Plenum Press, New York and London, pp. 63-138.

Haymon, R., Kastner, M., 1981. Hot spring deposits on the East Pacific Rise at 21°N: Preliminary description of mineralogy and genesis. *Earth and Planetary Science Letters* 53, 363-381.

Haymon, R. M., 1983. Growth history of hydrothermal black smoker chimneys. *Nature* 301, 695-698.

Herzig, P. M., Hannington, M. D., 2000. Polymetallic massive sulfide and gold mineralization at mid-ocean ridges and in subduction related environments. In: Cronan D.S. (Ed). *Handbook of Marine Mineral Deposits*. CRC Press, London, pp. 347-368.

Humphris S. E., Kleinrock M. C. 1996. Detailed morphology of the TAG active hydrothermal mound: Insights into its formation and growth. *Geophysical Research Letters* 23 (23), 3443-3446.

James R. H., Elderfield H., 1996. The Chemistry of ore-forming fluids and mineral precipitation rates in an active hydrothermal sulfide deposit on the Mid-Atlantic Ridge. *Geology* 24, 1147-1150.

Janecky, D.R., Seyfried W.E., 1984. Formation of massive sulfide deposits on oceanic ridge crests: incremental reaction models for mixing between hydrothermal solutions and sea water. *Geochimica et Cosmochimica Acta* 48, 2723-2738.

Kim, J., Lee, I., Lee, K., Yoo, C., Ko, Y., 2004. Formation of black and white smokers in the North Fiji Basin: Sulfur and lead isotope constraints. AGU Fall Meeting, 2004, Abstract No. B-13A-0192.

Kim, J., Lee, I., Halbach, P., Lee, K.Y., Ko, Y.T., Kim, K.H., 2006. Formation of hydrothermal vents in the North Fiji Basin: Sulfur and lead isotope constraints. *Chemical Geology* 233, 257-275.

Koski, R. A., Jonasson, I. R., Kadko, D. C., Smith, V. K., Wong, F. L., 1994. Compositions, growth mechanisms, and temporal relations of hydrothermal sulfide-sulfate-silica chimneys at the northern Cleft segment, Juan de Fuca Ridge. *Journal of Geophysical Research* 99 (B3), 4813-4832.

Lisitsyn, A.P., Malahoff, A.R., Bogdanov, Y.A., Soakai, S., Zonenshayn, L.P., Gurvich, Y.G., Murav'yev, K.G., Ivanov, G.V., 1992. Hydrothermal formations in the northern part of the Lau Basin, Pacific Ocean. *International Geology Review* 34 (8), 828-847.

Lisitsyn, A. P., Lukashin, V. N., Gordeev, V. V., McConachy, T. F., Scott, S. D., Shevchenko, V. P., 1997. Hydrological and geochemical anomalies associated with hydrothermal activity in SW Pacific marginal and back-arc basins. *Marine Geology* 142, 7-45.

Malahoff, A., Falloon, T., 1991. Preliminary Report of the Akademik Mstislav Keldysh/ Mir cruise 1990, Lau Basin Leg (May 7-21), on behalf of the Keldysh/Mir Science Team, SOPAC Cruise Report 137, 27 pp.

Marchig, V., 2000. Hydrothermal activity on the southern, Ultrafast-spreading segment of the East Pacific Rise. In: Conan, D.S. (Ed), *Handbook of Marine Mineral Deposits*. CRC Press, London, pp. 309-325.

Mills, R.A., Elderfield, H., 1995. Rare Earth element geochemistry of hydrothermal deposits from the active TAG Mound, 26°N Mid-Atlantic Ridge. *Geochimica et Cosmochimica Acta* 59, 3511-3524.

Mills, R. A., Wells D. M. and Roberts, S. 2001. Genesis of ferromanganese crusts from the TAG hydrothermal field. *Chemical Geology* 176, 283-293.

Moorby, S. A., Cronan, D. S., Glasby, G. P., 1984. Geochemistry of hydrothermal Mn-oxide deposits from the S.W. Pacific island arc. *Geochimica et Cosmochimica Acta* 48, 433–441.

Moorby, S. A., Cronan, D. S., 1981. The distribution of elements between co-existing phases in some marine ferromanganese-oxide deposits. *Geochimica et Cosmochimica Acta* 45, 1855-1877.

Morgan, J. W., Wandless, G. A., 1980. Rare earth element distribution in some hydrothermal minerals: Evidence for crystallographic control. *Geochimica et Cosmochimica Acta* 44, 973 – 980.

Murray, J. W., 1979. Iron oxides. In: Burns, R. G., (Ed.), *Marine Minerals*. Mineralogical Society of America, Washington, 47–98.

Natland, J.H., Rosendahl, B., Hekinian, R., Dmitriev, Y., Fodor, R.V., Goll, R.M., Hoffert, M., Humphris, S.E., Matthey, D.P., Peterson, N., Roggenthen, W., Schrader, E.L., Srivastava, R.K.,

Warren, N., 1979. Galapagos hydrothermal mounds: stratigraphy and chemistry revealed by deep-sea drilling. *Science* 204, 613-616.

Paerce J. A., Stern R. J., 2006. Origin of Back-Arc basin magmas: Trace element and isotope perspectives. In *Back-Arc Spreading Systems - Geological, Biological, Chemical and Physical Interactions* (Eds: Christie D.M., Fisher C.R., Sang-Mook L. and Sharon G.) pp. 70-73.

Paradis, S., Jonasson, I. R., Le Cheminant G. M., Watkinson, D. H., 1988, Two zinc-rich chimneys from the Plume Site, southern Juan de Fuca Ridge, *Canadian Mineralogist* 26, 637-654.

Parsons, L. M., Hawkins, J., Tiffin, D. L. 1989 Tectonics over 5Myr in the Lau back-arc Basin. *SW Pacific: New models from recent data. EOS* 73: 1366

Parson L. M., Tiffin D. L., 1993. Northern Lau Basin: Backarc extension at the leading edge of the Indo-Australian Plate. *Geo-Marine Letter* 13, 107-115.

Pichler, T., Veizer, J., 1999, Precipitation of Fe(III) oxyhydroxide deposits from shallow-water hydrothermal fluids in Tutum Bay, Ambitle Island, Papua New Guinea. *Chemical Geology* 162, 15-31.

Sawkins, F.J., 2009. Integrated tectonic-genetic model for volcanic-hosted massive sulfide deposits. *Geology* 18, 1061-1064.

Shanks, W. C. III, 2001. Stable isotopes in seafloor hydrothermal systems: vent fluids, hydrothermal deposits, hydrothermal alteration, and microbial processes. In: Valley, J.W., Cole, D.R. (Eds.), *Stable Isotope Geochemistry. Reviews in Mineralogy and Geochemistry* 43, 469–525.

Smith, W. H. F., 1993. On the Accuracy of Digital Bathymetric Data. *Journal of Geophysical Research Solid-Earth* 98 (B6), 9591-9603.

Stumm W., Morgan J. J. 1981. An introduction emphasizing chemical equilibria in natural waters. *Aquatic Chemistry* (Second edition), John Wiley and Sons, New York.

Tivey M. K. 1998. The Formation of Mineral Deposits At Mid-Ocean Ridges. *Oceanus*, 41, 22-26.

Tivey, M. K., Humphris, S. E., Thompson, G., Hannington, M. D., Rona, P. A., 1995 Deducing patterns of fluid flow and mixing within the TAG active hydrothermal mound using mineralogical and geochemical data. *Journal of Geophysical Research* 100 (B3), 12527-12555.

Usai, A., Someya, M. 1997. Distribution and composition of marine hydrogenetic and hydrothermal manganese deposits in the north-west Pacific. In: Nicholson, K., Hein, J. R., Buhn, B., Dasgupta, S. (Eds.), *Manganese Mineralization: Geochemistry and Mineralogy of Terrestrial and Marine Deposits*, Geological Society of London. Special Publication 119, 177-198.

Von Damm, K.L., 1995. Controls on the chemistry and temporal variability of sea floor hydrothermal fluids. In: Humphris, S.E., Zierenberg, R.A, Mullineaux, L.S., Thomson, R.E. (Eds.), *Sea Floor Hydrothermal Systems: Physical, chemical, biological and geological interactions*. Geophysical Monographs Series 91, American Geophysical Union, Washington DC, USA, pp. 222-247.

Wagner T., Cook N. J., 1998. Sphalerite remobilization during multistage hydrothermal mineralization events-examples from siderite-Pb-Zn-Cu-Sb veins, Rheinisches Schiefergebirge, Germany. *Mineralogy and Petrology* 63, 223-241.

Xiaotong, P., Huaiyang, Z. 2005. Growth history of hydrothermal chimneys at EPR 9-10°N: A structural and mineralogical study. *Science in China, Series D. Earth Sciences* 48, 1891-1899.

Figure Captions:

Figure 1. Bathymetry of Lau back arc basin, Southwest Pacific. Figure shows the four sites (M 2212/2218, M 2226, M 2231, M 2238) visited by 'MIR-1' and 'MIR-2' submersibles during the 19th cruise of R/V *Akademik Mstislav Keldysh*. The samples investigated are from site M-2226, located near the Kings Triple Junction. Bathymetric data is obtained from Smith (1993).

Figure 2. Schematic diagram of (A) the hydrothermal deposits, (B) the nearby second hydrothermal field named as “Christmas Tree” Field, from site M-2226 in northern Lau back-arc basin. (Modified after Lisitsyn et al., 1992). The numbers in parenthesis are the sample numbers studied in the present investigation.

Figure 3. Hydrothermal sulfides from northern Lau back-arc basin with their sub-samples. (A) The pedestal slab, M-2226-5 with four sections (L-1 to L-4), (B) The peripheral chimney section, M-2226-6/12 with six (S-1 to S-6) subsections and (C) the Fe and Mn oxide precipitate, M-2226-12 with two subsections (B-12 and O-12).

Figure 4. Chondrite (C-1) normalized rare earth element patterns of sub-samples from (A) pedestal slab, M-2226-5, (B) peripheral chimney, M-2226-6/12 and (C) Fe and Mn oxide precipitate, M-2226-12.

Table Captions:

Table 1. The minerals identified in three types of hydrothermal deposits (pedestal slab, peripheral chimney and Fe and Mn oxide precipitate) from KTJ, northern Lau back-arc basin.

Table 2. Major and trace element concentrations in different sections of pedestal slab, peripheral chimney and Fe and Mn oxide precipitate from KTJ, northern Lau back-arc basin.

Table 3. Geochemistry of rare earth element in different sections of pedestal slab, peripheral chimney and Fe and Mn oxide precipitate from KTJ, northern Lau back-arc basin.

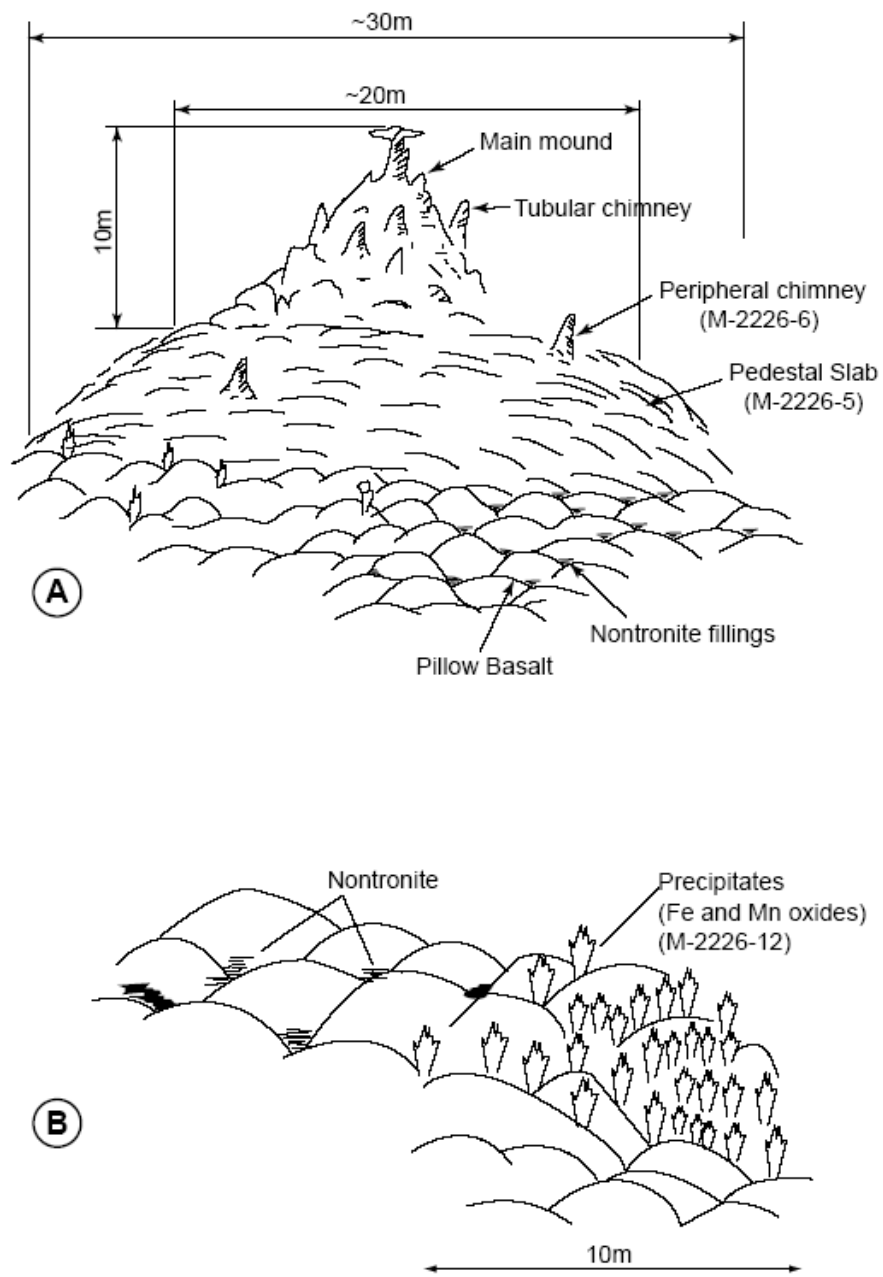


Figure-2.



Figure - 3.

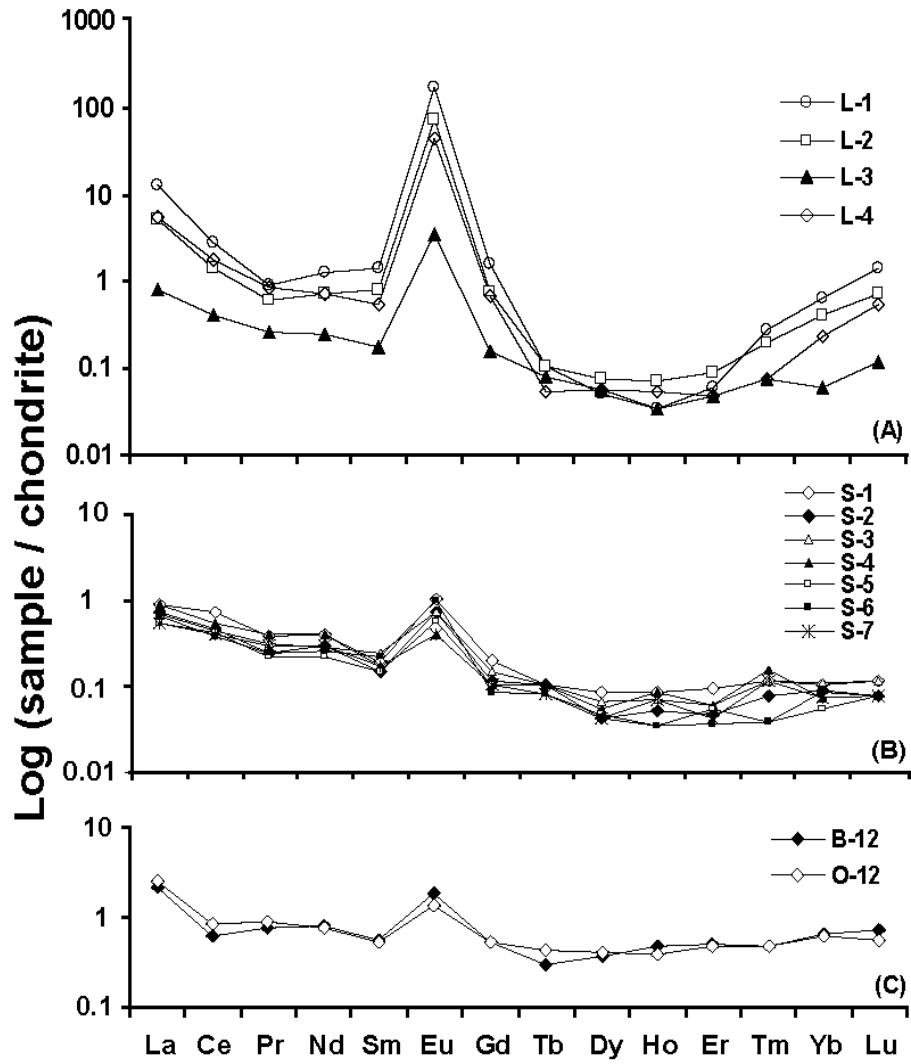


Figure- 4

Table-1

Samples	Subsections	Minerals	
		Major	Minor
Pedestal slab (M2226-5)	L-1, L-2.	Chalcopyrite, Barite, Pyrite.	Sphalerite, Wurtzite, Manganosite.
	L-3	Sphalerite.	Chalcopyrite, Pyrite, Manganosite.
	L-4	Chalcopyrite, Pyrite.	Sphalerite.
Chimney (M2226-6)	S-1, S-2, S-3, S-4, S-5, S-6.	Sphalerite.	Pyrite, Chalcopyrite.
Precipitate (M2226-12)	B-12	Birnessite	
	O-12	X-ray amorphous	

Table-2

Element	Pedestal slab (M2226-5)				Peripheral chimney (M2226-6)						Precipitate (M2226-12)	
	L-1	L-2	L-3	L-4	S-1	S-2	S-3	S-4	S-5	S-6	B-12	O-12
Mn (%)	0.02	0.01	0.03	0.02	0.03	0.06	0.04	0.04	0.03	0.03	32.2	0.09
Fe	8.09	8.6	2.87	12.5	1.73	1.53	4.37	1.18	1.39	1.84	1.33	14.5
Cu	7.39	11.4	4.48	16.4	1.54	1.52	1.08	1.22	1.05	1.1	0.01	0.01
Zn	1.14	2.25	23.9	7.29	32.8	25.6	23.8	34	29.2	28	0.18	0.01
Sc (ppm)	0.29	0.29	0.28	1.55	5.1	1.03	0.54	0.38	0.36	0.36	0.32	0.33
V	3.73	6.62	8.54	10.5	24.8	29	23.9	13.1	11.9	11.1	4.52	10.6
Co	0.49	0.48	0.45	0.45	0.65	0.6	0.72	0.49	0.71	0.5	1.56	3.83
Ni	16.6	14.7	17.8	14.5	22.3	16.1	22	19.3	22.2	17.6	87.4	15.6
Ga	2.7	9.5	94.6	45.2	76.9	72.8	51.9	57.2	21.8	11.8	12.6	3.95
Rb	1.63	1.36	0.46	0.31	1.51	1.72	1.66	0.99	1.02	1.09	2.95	2.54
Sr	181	70.4	4.83	110	5.58	4.56	4.62	2.28	2.8	2.9	70	56.2
Y	0.22	0.24	0.09	0.13	0.14	0.09	0.13	0.14	0.11	0.09	0.9	1.09
Zr	0.46	0.77	0.44	1.06	6.3	1.91	5.7	5.86	1.51	2.88	0.81	1.61
Nb	0.1	0.51	0.08	0.27	0.15	0.39	0.31	1.62	0.11	0.27	0.03	0.09
Ag	8.65	7.24	15.5	14.4	35.4	19.9	20.2	13.5	12.1	21.6	0.25	1.5
Cs	1.97	1.3	0.2	0.4	0.07	0.09	0.08	0.05	0.06	0.06	0.02	0.04
Ba	10295	4163	95.8	2698	31.4	24.9	20.4	9.63	12.9	26.1	31.9	21.4
Hf	0.05	0.04	0.02	0.06	0.23	0.1	1.69	0.27	0.09	0.16	0.03	0.07
Ta	0.02	0.07	0.01	0.22	0.79	0.64	0.09	0.08	0.01	0.02	0.07	0.02
Au	1.49	1.87	2.82	1.91	5.76	2.31	2.01	1.84	1.57	3.01	2.07	1.02
Th	0.17	0.12	0.13	0.1	0.18	0.15	0.12	0.31	0.08	0.13	0.09	0.15
U	0.11	0.09	0.05	0.09	0.22	0.16	0.21	0.17	0.15	0.23	1.85	0.45
Mn/Fe	0.002	0.001	0.01	0.001	0.017	0.039	0.009	0.034	0.021	0.016	24.2	0.006
Ba/Nb	>10 ⁵	10 ⁴	10 ³	10 ⁴	209.7	63.7	65.7	5.9	117.3	96.6	10 ³	237

Table- 3

Concentration of REE (ppm)	Pedestal slab (M2226-5)				Peripheral chimney (M2226-6)						Precipitate (M2226-12)	
	L-1	L-2	L-3	L-4	S-1	S-2	S-3	S-4	S-5	S-6	B-12	O-12
La	3.215	1.321	0.203	1.324	0.225	0.181	0.169	0.217	0.131	0.161	0.531	0.637
Ce	1.789	0.906	0.269	1.145	0.464	0.295	0.28	0.345	0.274	0.252	0.4	0.534
Pr	0.09	0.06	0.025	0.083	0.038	0.024	0.031	0.039	0.022	0.024	0.074	0.086
Nd	0.613	0.35	0.12	0.348	0.196	0.14	0.138	0.189	0.105	0.125	0.391	0.372
Sm	0.215	0.126	0.028	0.085	0.029	0.023	0.038	0.027	0.023	0.034	0.085	0.083
Eu	9.912	4.332	0.21	2.655	0.06	0.042	0.042	0.023	0.034	0.059	0.107	0.078
Gd	0.334	0.161	0.033	0.137	0.042	0.024	0.031	0.022	0.022	0.018	0.111	0.107
Tb	0.004	0.004	0.003	0.002	0.004	0.004	0.004	0.004	0.003	0.003	0.011	0.016
Dy	0.013	0.019	0.015	0.015	0.022	0.011	0.017	0.014	0.012	0.011	0.096	0.106
Ho	0.002	0.004	0.002	0.003	0.005	0.003	0.004	0.005	0.002	0.002	0.027	0.022
Er	0.01	0.015	0.008	0.008	0.016	0.008	0.01	0.01	0.009	0.006	0.084	0.078
Tm	0.007	0.005	0.002	0.002	0.003	0.002	0.003	0.004	0.001	0.001	0.012	0.012
Yb	0.108	0.067	0.01	0.039	0.017	0.015	0.018	0.012	0.009	0.014	0.107	0.103
Lu	0.037	0.019	0.003	0.014	0.003	0.002	0.003	0.002	0.002	0.002	0.019	0.014
Σ REE(ppm)	16.3	7.39	0.93	5.86	1.12	0.77	0.79	0.91	0.65	0.71	1.66	1.88
Nd _n /Yb _n	1.98	1.82	4.18	3.11	4.02	3.25	2.67	5.49	4.07	3.11	1.27	1.26
Eu _n /Sm _n	122	91.2	19.9	82.9	5.49	4.85	2.93	2.26	3.9	4.6	3.34	2.49
^a Ce/Ce*	0.31	0.37	0.66	0.47	0.97	0.78	0.78	0.74	0.99	0.75	0.36	0.42

$${}^a\text{Ce/Ce}^* = 3\text{Ce}_n / (2\text{La}_n + \text{Nd}_n)$$